

The Effect of Ionization on Cluster Formation in Laser Ablation Plumes

M. S. Tillack, D. Blair and S. S. Harilal

August 21, 2003



**Fusion Division
Center for Energy Research**

University of California, San Diego
La Jolla, CA 92093-0417

The effect of ionization on cluster formation in laser ablation plumes

M. S. Tillack, D. Blair and S. S. Harilal

Abstract

Ablation plumes caused by short-pulse laser irradiation provide conditions which are well suited to the formation of nanoclusters. The high saturation ratios and presence of ionization lead to extraordinarily high nucleation rates and small critical radii. We have explored the homogeneous nucleation and heterogeneous growth of condensate from Si targets expanding into a low-pressure He ambient using a Nd:YAG laser with pulse length of 8 ns, wavelength of 532 nm and intensities in the range of 5×10^7 to 5×10^9 W/cm². Clusters in the range of 5–50 nm have been produced. In the highly dynamic, non-linear regime of short-pulse laser-matter interactions, plume evolution and condensation processes are strongly coupled and difficult to predict accurately from modeling alone. Both numerical predictions and experimental results were used to quantify the competing effects of ionization and supersaturation. The results suggest a dominant influence of ionization for nearly all intensities above the ablation threshold.

I. Introduction

The interaction of laser ablation plumes with a background gas has received increased attention recently due to its importance in pulsed laser deposition [1], nanoparticle formation and growth [2-4], and laser micromachining [5]. Compared with expansion into a vacuum, the interaction of the plume with an ambient gas is a far more complex gasdynamic process due to the rise of new physical processes involved such as deceleration, thermalization of the ablated species, interpenetration, recombination, formation of shock waves and clustering [6-11].

Short-pulse laser irradiation of surfaces initiates a complex sequence of events which occur both during and after the laser pulse. As depicted in Figure 1, this includes laser absorption in the surface, phase change and mass expulsion in both liquid and vapor states, plasma formation leading to partial absorption in the plume, acceleration of the vapor to hypersonic velocity followed by rapid condensation and finally, in cases with sufficiently high ambient pressure, collapse of the plume remnants onto the surface. During the expansion stage, the plume front can achieve very high velocities. For example, the expansion velocity obtained with a laser intensity of 10^9 W/cm² can easily reach 10^8 cm/s, corresponding to a directed kinetic energy greater than 1 keV [12-14].

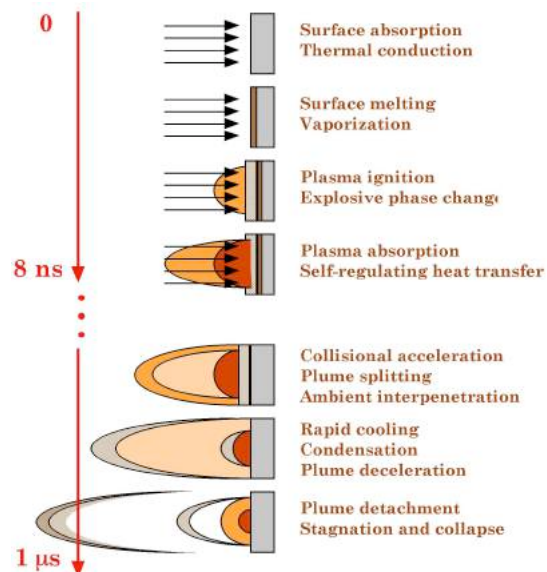


Figure 1. Stages of laser ablation plume creation, expansion and condensation

Expansion of the saturated vapor, combined with heat transfer at the contact surface between the plume and the ambient gas, leads to very rapid cooling. This cooling can occur more rapidly than condensation, leading to exceptionally high saturation ratio S , where S represents the ratio of the actual vapor pressure to the saturation pressure at a given temperature: $S = p_v/p_s$.

According to classical condensation theory, the rate of homogeneous nucleation of condensate is strongly dependent on the saturation ratio obtained. The free energy of formation of condensate is determined from a balance between bulk cohesive forces between liquid atoms and an energy barrier due to surface tension. In terms of the cluster radius r , the free energy to form a spherical condensed cluster can be written as [15-17]:

$$W(r) = -\frac{4}{3}\pi r^3(n\Delta\mu) + 4\pi r^2\sigma \quad (1)$$

where $\Delta\mu = kT\ln S$ is the difference in chemical potential between the condensed and uncondensed atoms, σ is the surface tension (~ 0.73 N/m for Si), and n is the atom number density. Figure 2 shows an example of the Gibbs free energy vs. spherical cluster radius for Si at 2000°K and $n=10^{20}/\text{cm}^3$. The critical radius r^* , beyond which growth becomes energetically preferred, occurs at the maximum of $W(r)$:

$$r^* = \frac{2\sigma}{n\Delta\mu} \quad (2)$$

The rate of homogeneous nucleation (J_h) is proportional to the concentration of critical clusters (C^*), the monomer attachment frequency (Γ) and the Zel'dovich prefactor (Z) which accounts for the statistical probability that an impingement will push a critical cluster over the barrier:

$$J_h = Z \Gamma C^* \quad (3)$$

where Z is given by:

$$Z = \sqrt{\Delta W_k / 3\pi k T N_k^2} \quad (4)$$

ΔW_k is the nucleation work – i.e., the size of the barrier – and N_k is the number of atoms in a critical cluster. The concentration of critical clusters is also related to the size of the barrier, and is given by [18]:

$$C^* = \frac{p}{kT} \exp\left(-\frac{\Delta W_k}{kT}\right) \quad (5)$$

Figure 3 shows the resulting homogeneous nucleation rate. For the parameters in Figure 2, the barrier in the absence of ionization is approximately $25kT$.

It is well known that charged ions tend to be jacketed by surrounding neutral atoms [16,18]. As a result of dielectric forces, a local minimum energy state exists, corresponding to this jacketed

ion, and the critical radius shifts to a smaller value. In addition, the energy barrier is lowered, leading to a higher homogeneous nucleation rate at any given temperature. The free energy is modified in the presence of ionization to account for this dielectric energy:

$$W(r) = -\frac{4}{3}\pi r^3(n\Delta\mu) + 4\pi r^2\sigma + (1 - 1/\epsilon_c)(Q^2/8\pi\epsilon_o)(1/r - 1/r_a) \quad (6)$$

where ϵ is the dielectric constant of the clusters, Q is the ionic charge, r_a is the radius of a jacketed ion, and we assume $\epsilon=1$ for the vapor phase. The critical radius is obtained by differentiating eqn. 6, and the nucleation rate is obtained by substituting this modified W into eqn. 3–5.

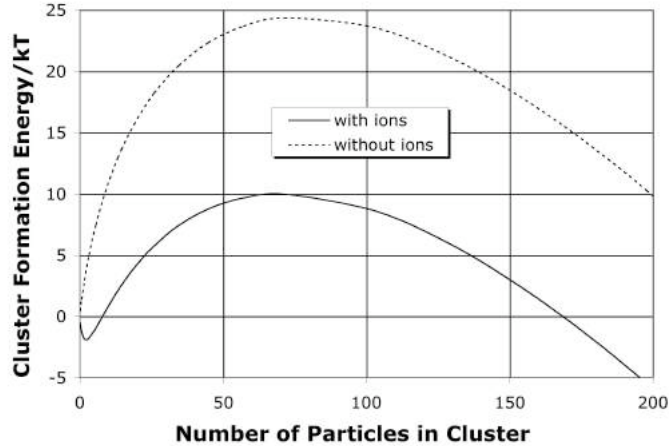


Figure 2. Free energy of cluster formation for Si at 2000 K and $n=10^{20}/\text{cm}^3$ compared with the same conditions with $Z_{\text{eff}}=0.01$.

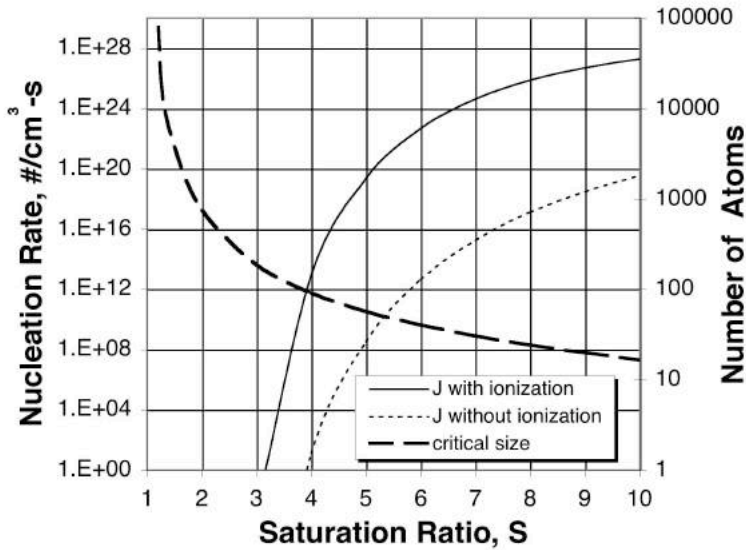


Figure 3. Homogeneous nucleation rate both with and without ionization for the same parameters as Figure 2.

These effects are depicted in Figures 2 and 3, which are based on the same conditions described above, but with 1% ionization ($Z_{\text{eff}}=0.01$). Note, ionization reduces the energy barrier substantially, leading to much higher nucleation rates owing to the exponential dependence on $\Delta W/kT$.

At sufficiently high saturation ratio, the heterogeneous nucleation on ions can become “barrierless”, such that the rate is determined only by the concentration of seed sites. In this regime, if the saturation ratio continues to increase, the homogeneous nucleation rate eventually will overtake the ion seed pathway [16]. An understanding of this competition between ion-induced nucleation and homogeneous nucleation at high saturation ratio is not firmly established, especially within the context of laser ablation plumes.

In this work we have studied the mechanisms of cluster formation in laser plasma. Previous measurements of laser plasma have shown that non-equilibrium ionization may exist throughout the duration of cluster formation and growth [19,20]. A mechanism for the role of ions in condensation has been proposed by previous investigators [18], however, this model has not been applied to short-pulse laser plasma, and cannot be applied properly without verifying that the assumptions behind it are valid. Numerical simulations also have been used to model the laser plasma flow [21–25]; however, none has investigated the role of ions in the condensation of the laser plasma.

We explored regimes of laser intensity from 5×10^7 to 5×10^9 W/cm² which provide average charge state between 0.001 and 1 (fully ionized Si would be 14). The background gas is an important contributor to the processes of expansion and condensation, but was not studied extensively; for all cases considered here we used He at 500 mTorr.

We have found that the amount of ionization required to provide an important influence on the condensation physics (as compared with classical supersaturation-driven condensation) is very low, and can be reached with laser intensities very near the ablation threshold. We conclude that the ion seed pathway is an important consideration for nearly all laser ablation plumes.

Laser ablation plumes are highly dynamic, non-linear, and provide strong coupling between the basic expansion dynamics and the processes involved in condensation. In order to provide a qualitative understanding of the time-evolution of condensation within an ablation plume, a one-dimensional model of laser ablation plume behavior was developed. Key features of the model are summarized in Section II and example results are shown in Section III. Experiments were performed in order to directly measure the final size distribution of clusters and to provide data for a better understanding of the underlying physics. Four primary types of measurements were made: (1) plume expansion dynamics, (2) plasma temperature and density, which are then used to estimate saturation ratio and ionization state, (3) spectroscopic emission from Si₂ dimers and its correlation with Si⁺ ions, and (4) final cluster size distribution. Further details on experimental results are provided in Section IV. Finally, Section V provides a summary and conclusions derived from these experimental and modeling studies.

II. Model Description

One of the unique aspects of condensation in laser ablation plumes is the highly dynamic nature of the plume state variables, upon which the condensation depends strongly and nonlinearly. Changes occur over many orders of magnitude during the event and across the spatial domain. In order to provide a qualitative understanding of the evolving plume state variables and to help guide and interpret experimental studies, a numerical model of laser ablation plume behavior was developed. The model includes all of the basic mechanisms that govern the expansion of the vapor and the subsequent condensation. Simplifications are made in several areas where the impact is believed to be small, in order provide a relatively robust scoping tool focused on only the key physics. The fluid equations are one-dimensional in the direction of the plume expansion. The model treats the various steps in the expansion summarized in [Section I](#), including laser absorption, surface thermal response, mass evolution, plasma ionization and recombination, gas-phase hydrodynamics and heat transfer, and aerosol generation and growth. Mechanisms for aerosol ejection directly from the surface have not been treated in this work.

Absorption in the surface. Laser absorption is modeled with a surface attenuation coefficient [5]. A fraction of the incident energy flux, I_o , is reflected and the remainder is deposited volumetrically according to the Lambert Beer law:

$$I(z) = I_o \square e^{-\square z} \quad (7)$$

Thermal response of the surface. The thermal response of the surface includes both heat capacity and phase change energies. The governing energy equation is given by:

$$\square \partial^2 T(z,t)/\partial z^2 + I_o(t) \square e^{-\square z} = \square C_p \partial T(z,t)/\partial t \quad (8)$$

except at the surface, where the energy balance includes the energy flux from the surface into the flow space [24]:

$$q_{sf} = u(\square Q_v + E + \square u^2/2 + p_s) \quad (9)$$

Here u is the vapor velocity, Q_v is the heat of evaporation, and E is the internal energy above the saturation temperature.

Mass evolution from the surface. The vapor pressure at the surface is estimated *via* classical thermodynamic relations between temperature and vapor pressure [26]:

$$p_s = p_o \exp[Q_v/(kT_b) - Q_v/(kT_s)] \quad (10)$$

where T_b is the boiling temperature of the target material at the ambient pressure p_o , k is the Boltzmann constant and T_s is the target surface temperature at the melt-vapor interface. The mass flux is given by:

$$J = \sqrt{m/2\pi k} \left(\Gamma \frac{\sigma_c p_g}{\sqrt{T_g}} - \frac{\sigma_e p_{sat}}{\sqrt{T_f}} \right) \quad (11)$$

where Γ is a Maxwellian factor, m is the atomic mass, and the coefficients σ_e and σ_c are evaporation and condensation coefficients.

During the laser pulse, the rapid evaporation will result in a Knudsen layer at the surface, where translational equilibrium is not yet reached [21]. The resulting jump in parameters was not modeled in detail because the long time-scale evolution of the plume is not significantly affected by this short-term near-surface effect.

Plasma ionization, recombination and absorption of light. As the vapor pressure begins to build up, ionization can be initiated either through direct heating or by a collisional cascade of electrons in the strong electric field of the laser – *i.e.*, laser-induced breakdown. The laser intensities utilized in our work (of the order of 10^9 W/cm²) are well below the breakdown threshold of most gases [22], such that ionization is assumed to be dominated by thermal effects.

We estimated the ionization state using a density-corrected Saha equation [23]:

$$\frac{n_{r+1} n_r}{n_r} = 2 \frac{U_{r+1}}{U_r} \left(\frac{2\pi m_e k T}{h^2} \right)^{3/2} \exp \left(-\frac{I_r^{eff}}{kT} \right) \quad (12)$$

Peak values range from 0.001 to 1.0 for laser intensities from 5×10^7 to 5×10^9 W/cm².

The resulting plasma in front of the surface will absorb a fraction of the incident laser light during the pulse. This absorption occurs by inverse bremsstrahlung with attenuation length given by [15]:

$$\kappa = 6.52 \times 10^{-24} Z^2 \left(\frac{n_i n_e}{T^{7/2}} \right) [cm^{-1}] \quad (13)$$

For the laser intensities considered here, less than 1% of the incident light is absorbed by inverse bremsstrahlung.

Recombination rates are relatively slow during the later stages of plume expansion, and are modeled using a rate equation instead of assuming ionization equilibrium [15]:

$$\frac{dx}{dt} = bn(x_{eq}^2 - x^2) \quad (14)$$

where $x = n_e/n$ is the degree of ionization, x_{eq} is the equilibrium ionization given by the Saha equation, and b is the rate constant (a function of n and T).

Vapor and ambient hydrodynamics. The rapidly increasing vapor pressure near the surface creates a large driving force for vapor expansion. The high temperature and density lead to pressures far exceeding the background gas pressure (of the order of 10–100 atm).

In order to solve for the ensuing plume dynamics, a set of one-dimensional two-fluid equations was used. These consist of mass conservation laws for both the vapor and the background gas, and a single momentum conservation law for the mixture:

$$\frac{\partial \rho_v}{\partial t} + \frac{\partial (\rho_v u)}{\partial z} = \frac{\partial}{\partial z} \left(\rho D_{ab} \frac{\partial w_v}{\partial z} \right) - m_v I_n \quad (15)$$

$$\frac{\partial \rho_b}{\partial t} + \frac{\partial (\rho_b u)}{\partial z} = - \frac{\partial}{\partial z} \left(\rho D_{ab} \frac{\partial w_v}{\partial z} \right) \quad (16)$$

$$\frac{\partial \rho u}{\partial t} = - \frac{\partial (\rho u u)}{\partial z} - \frac{\partial}{\partial z} \mu \frac{\partial u}{\partial z} - \frac{\partial p}{\partial z} \quad (17)$$

As the laser ablation plume expands into a low-pressure background gas, eventually the density becomes so low that the flow is no longer in a continuum regime. Based on our experience, at or before 1 μ sec the Knudsen number reaches 0.1, which is a commonly accepted value at which the mean free path is too long to justify a fluid approximation. Most of the condensation physics is completed at this point in time, such that we did not attempt to adjust the flow calculations. Other researchers (*e.g.*, [30]) have developed hybrid models which take into account scattering and interpenetration.

For simplicity the condensate was not modeled separately in the fluid dynamic calculation. It was assumed that the condensate travels at the same velocity as the vapor/gas mixture and shares the same temperature. In addition, it was assumed that the condensate does not alter the transport properties of the vapor.

Energy conservation in the flow space. The heat transfer and thermal response in the flow space are described by an energy conservation equation for the vapor/gas mixture. It accounts for the change in internal energy, transport and sources and sinks of energy:

$$\frac{\partial e}{\partial t} + u \frac{\partial e}{\partial z} = - \frac{\partial q}{\partial z} + \mu \left(\frac{\partial u}{\partial z} \right)^2 + \left(\frac{\partial p}{\partial t} + u \frac{\partial p}{\partial z} \right) + Q_v I_n + q_{ib} + q_r \quad (18)$$

The internal energy includes the ionization energy, and the sources include condensation ($Q_v I_n$), laser absorption during the pulse (q_{ib}) and recombination (q_r). The addition energy source from the liquid surface is included at the boundary, as described above.

Homogeneous nucleation and heterogeneous growth of condensate. The homogeneous nucleation rate is evaluated using the expressions in [Section I](#). The growth of pre-existing clusters is modeled using surface condensation rates (J_s) obtained from the Knudsen formula and Clausius-Clapeyron relation ([eqs. 10 and 11](#) are valid for condensation as well as evaporation). Agglomeration (or breakup) by cluster collisions is assumed to be small. Then the total rate of

nucleation (number of vapor molecules condensed per unit volume per unit time) is given by a sum of homogeneous creation of critical clusters and agglomeration on pre-existing clusters [23]:

$$I = 4\pi J_s \int_0^\infty F(R) R^2 dR + \frac{4}{3} \pi r^*{}^3 n J_h \quad (19)$$

In order to obtain the spatial distribution of the condensed phase numerically, the condensate distribution function is described as a system of moments, for which a series of transport equations was solved. Following Gnedovets [23], a particulate transport equation is transformed to an infinite set of moment equations by multiplying by R^k and integrating over cluster radius from zero to infinity to give a set of moment equations which relate particulate nucleation and growth rates to the condensate size distribution, taking into account cluster transport in the plasma.

Solution methodology. Numerically, the above set of equations was solved using an explicit Euler scheme with forward stepping in time. Spatial derivatives were approximated with simple upwind differencing to avoid oscillations in the solution, which can result in singularities in the condensation model. Each node in the domain is assumed to have constant properties for both the vapor and fluid, and a single condensate number density and mean radius which is governed by the growth rate equations. A von Nuemann stability analysis was performed and used to calculate appropriate time steps, which enabled stable solutions to be generated [31].

III. Modeling Results

A representative example is described here to illustrate the main features of expansion and condensation. The target is silicon and the background gas is helium, initially at room temperature and 500 mTorr pressure. [Figure 4](#) shows the laser intensity and surface temperature response. The incident 532-nm laser pulse is Gaussian in time with a full width half maximum of 5 ns and average intensity of 25 GW/cm². The surface temperature rises while the laser is on, and then drops rapidly following the termination of the pulse. During this temperature excursion, the melting point (1420°C) is quickly reached and the saturation pressure of Si rises rapidly, such that a violent expansion into the low-pressure background gas is initiated.

[Figure 5](#) shows example density profiles for both the target vapor and He background gas at several times into the event. The initial pressure of $\sim 10^{19}/\text{cm}^3$ combined with a vapor temperature of 12,000 K leads to an initial pressure of the order of 15 atm. Initially, the background gas is expelled from the wall. A small amount of interpenetration occurs due to the finite diffusivity of He in Si. As the plume continues to expand, the “contact surface” extends out further and further into the background gas. By 500 ns, rapid vapor condensation occurs both at the cooled wall and by nucleation and growth in the flow space, leading to a rapid collapse of the vapor density. At this point in time, the plume has pushed about 1.5 cm away from the wall, which is consistent with our experimental measurements ([see Section IV](#)). A void region forms because the condensation occurs more rapidly than the back flux of helium. Our continuum flow model breaks down in this regime, when the plume Knudsen number exceeds 0.1, such that we terminated the model before the background gas collapsed back into the wall.

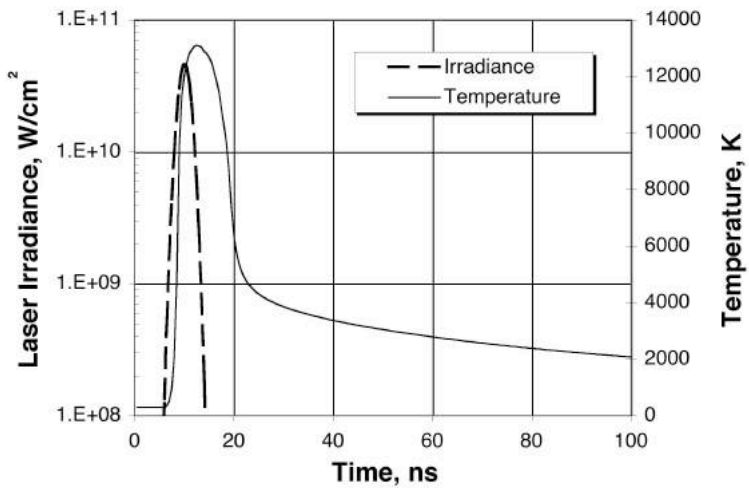


Figure 4. Laser irradiance and surface temperature response.

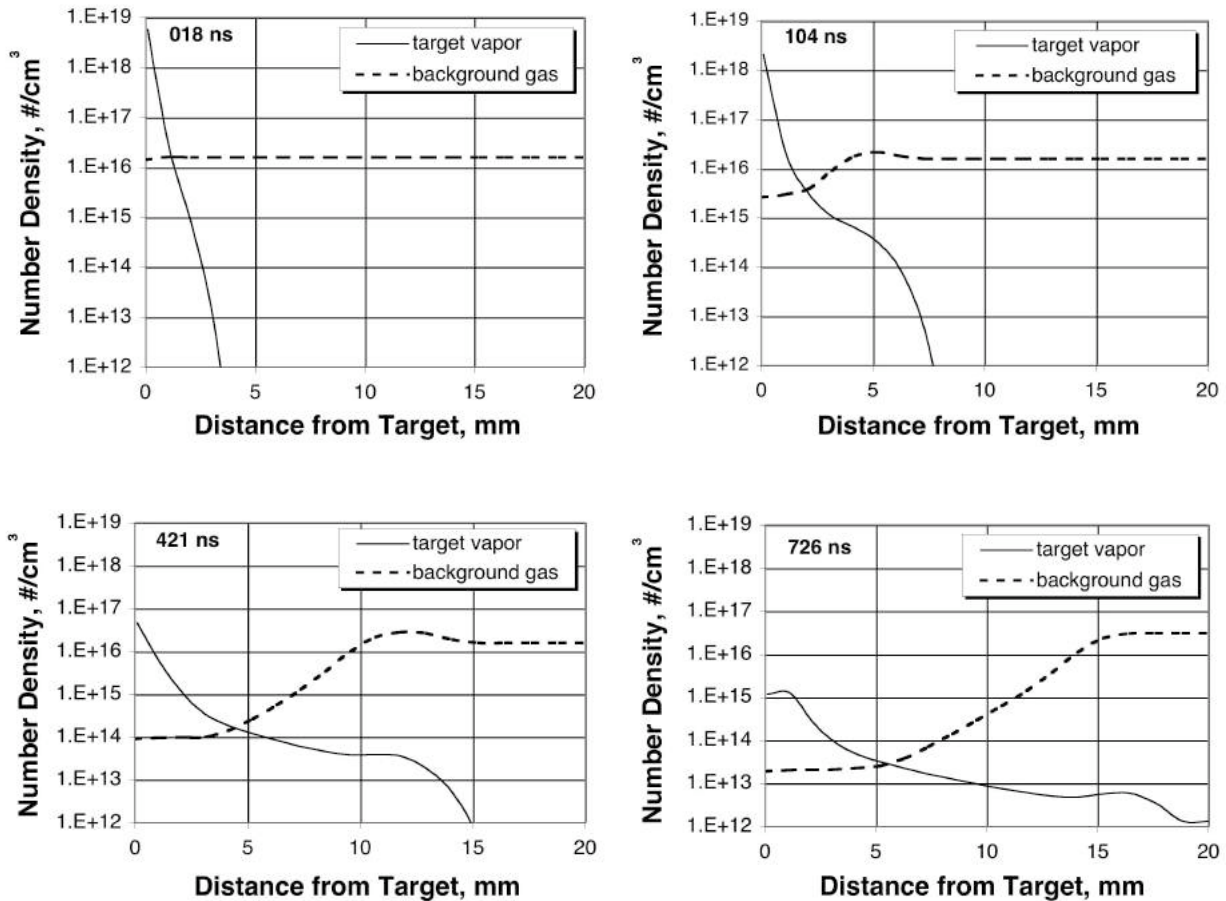


Figure 5. Spatial distribution of vapor and background gas density at various times in the plume expansion.

[Figure 6](#) shows the corresponding velocity profiles. (The background gas and vapor are treated as a single fluid in the momentum equation.) After the laser pulse has terminated, the model predicts that the vapor velocity is 15 km/s. A peak velocity of 35 km/s is achieved at about 100 ns following the pulse, as a result of continued influx of vapor into the plume and the transfer of thermal energy into directed kinetic energy. After 100 ns, the velocity rapidly falls to values below 1 km/s. These values are consistent with experimental measurements by ourselves and others [12–14].

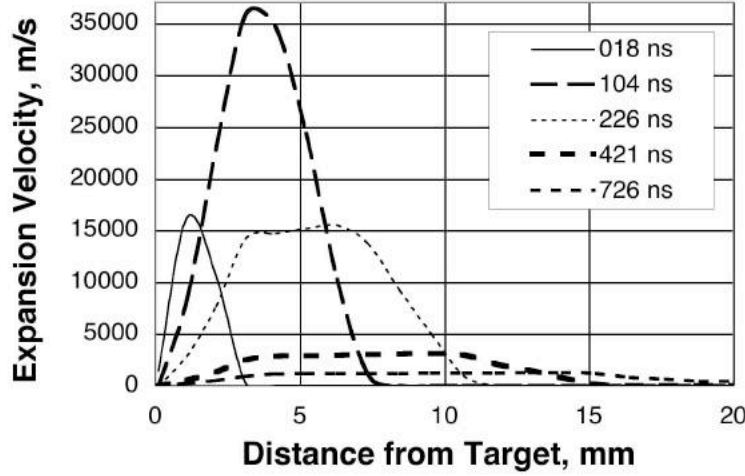


Figure 6. Velocity profile at various times in the plume expansion.

[Figure 7](#) depicts the temporal evolution of the ionization fraction (n_e/n_o) vs. time in the vicinity of the target surface. The ionization state increases rapidly as the temperature rises, following the Saha equation (eqn. 12). After termination of the pulse, the ionization fraction drops off more slowly than the temperature due to the rate limited behavior of recombination (eqn. 14). A peak value of ~ 0.02 is reached at the end of the laser pulse.

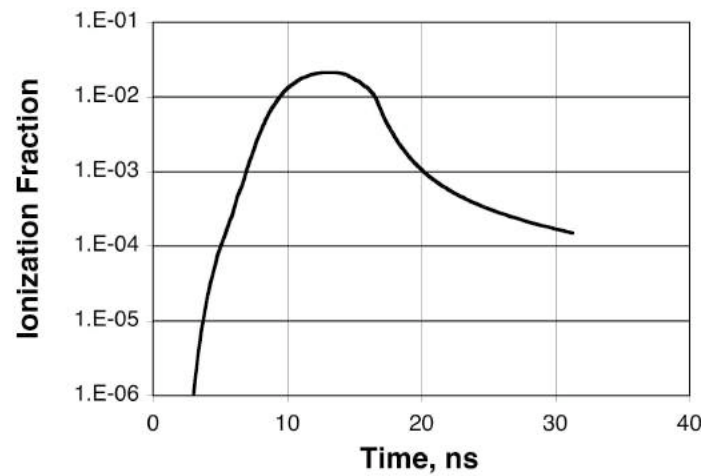


Figure 7. Charge state evolution vs. time near the target surface

[Figure 8](#) shows the temporal behavior of the saturation ratio (p_v/p_s) averaged over the plume for laser intensities ranging from 0.5 to 50 GW/cm². The spike in saturation ratio occurs much

quicker for higher intensities, which is probably due to the higher vapor pressures and faster expansion rates. It also drops more quickly at higher intensities.

The peak value of saturation ratio is significantly reduced at higher laser intensities. This likely occurs due to a combination of several effects. Condensation is reduced at elevated intensities due to the higher cluster temperature, increased heating of clusters in the plume by recombination, and the high expansion velocity which rapidly creates a very low vapor pressure in the plume. The saturation ratio will decrease any time the product of the vapor density and vapor temperature falls more rapidly than the saturation pressure at the cluster surface.

Figure 9 shows the resulting average cluster size at the end of the expansion. In order to highlight the effect of ionization, cases were run with the ionization artificially set to zero. At the lowest intensity (0.05 GW/cm^2) the amount of ionization is too small to affect the particle sizes. However, for higher values the presence of ionization is predicted to significantly decrease the particle sizes, in agreement with the predictions from Section I. As the laser intensity increases, the average particle size decreases either with or without the presence of ionization.

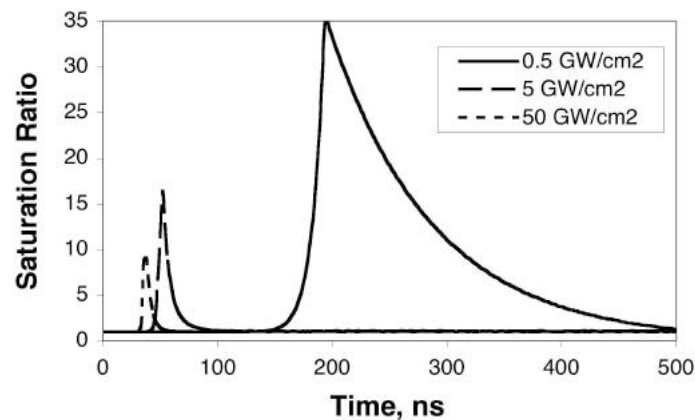


Figure 8. Predicted evolution of the plume-averaged saturation ratio *vs.* time for several laser intensities.

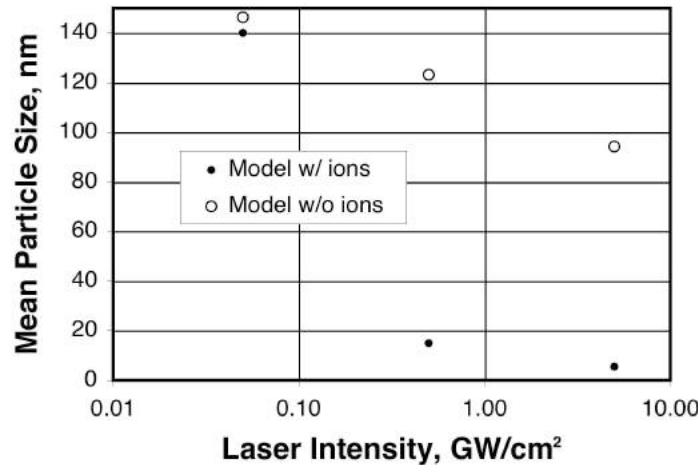


Figure 9. Comparison of the predicted mean particle size after 500 ns both with and without ionization considered.

IV. Experimental Measurements

In this section we summarize the experimental measurements of both the plume state variables and the final size distribution of condensate. Three primary experimental investigations were performed:

1. A gated ICCD camera was used to image visible emission from the expanding plume.
2. Spectroscopy was used to measure T and n , which were then used to calculate Z_{eff} and S . Dimer spectroscopy also was performed in order to determine the time and location at which clustering begins.
3. Atomic force microscopy on atomic flatness witness plates was used to measure the final condensate distribution.

[Figure 10](#) shows a schematic of the experimental setup. Pulses from a frequency-doubled Q-switched Nd:YAG laser were used to create Si ablation plumes in a stainless steel vacuum chamber with base pressure $\sim 10^{-8}$ Torr. Injection seeding maintains a reproducible pulse with 8 ns full-width half-maximum. The laser intensity was varied by attenuating the incident pulse energy using a polarizing cube and waveplate. The spot size was kept constant for all intensities. The average laser intensity was measured using an energy meter and post-examination of the crater size. Single-crystal Si targets were rotated about an axis parallel to the beam in order to improve shot-to-shot reproducibility and to avoid drilling. Further details on the diagnostic techniques are provided in the subsections below.

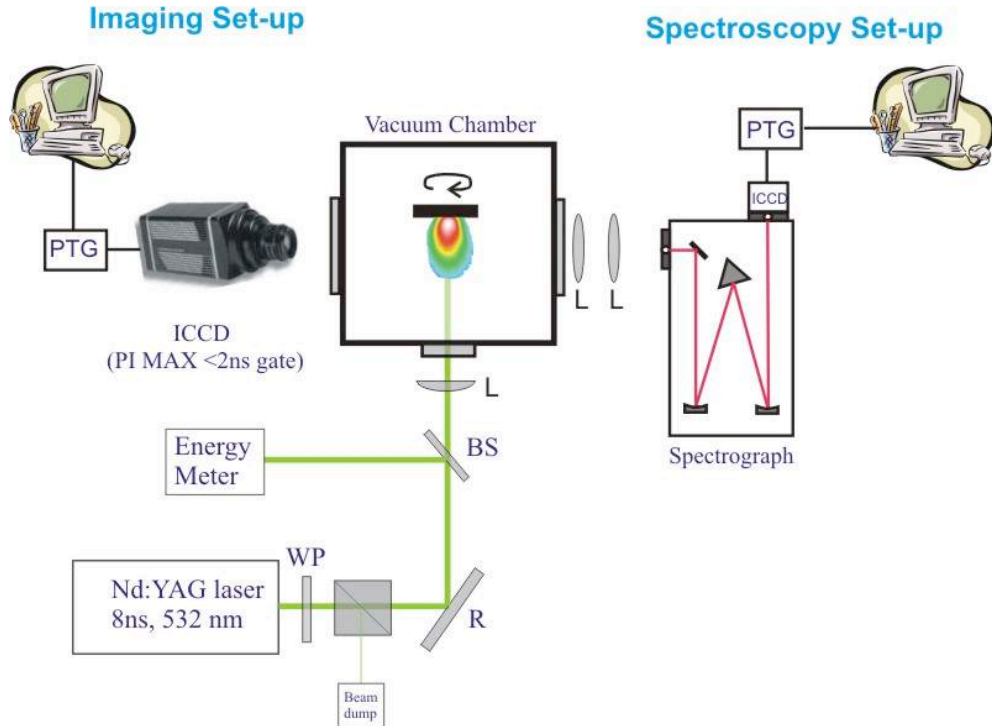


Figure 10. Chamber and diagnostic layout for ablation experiments (PTG, Programmable Timing Generator; WP, wave plate; R, reflector; BS, beam sampler; L, lens).

IV.a. Expansion dynamics

Imaging of the ablation plume provides an estimate of the expansion velocity as well as details on the internal structure. We utilized an intensified CCD camera (Roper PiMax model 512RB) located orthogonal to the plasma expansion direction for photographing the plume at different times after the evolution. 2 ns gating was used to capture the images at times <200 ns and a wider gate (10 ns) was used for times > 200 ns. The emission from the plasma was recorded integrally in the wavelength range 350–900 nm. In order to eliminate stray photons from the 532-nm laser light from reaching the camera, a magenta subtractive filter was used. A programmable timing generator was used to control the delay time between the laser pulse and the imaging system with overall temporal resolution of 1 ns.

[Figure 11](#) shows a sequence of images collected by delaying the gate by different amounts relative to the laser pulse. Each image is captured from a single laser pulse. A movie can be constructed by adding together the images from several sequential pulses using increasing delay time. The smoothness of the plume evolution attests to the reproducibility of the data.

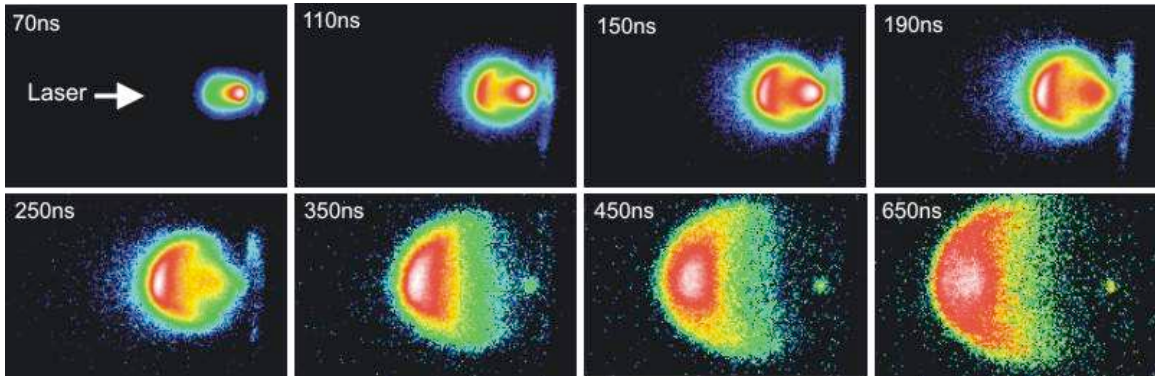


Figure 11. ICCD photographs of visible emission from laser-produced Si plasma at 5 GW/cm^2 average laser intensity and 500 mTorr He background gas. The timings in the images represent the time after the onset of plasma formation. All of the images are normalized to their maximum intensity. Plume behavior indicates free expansion.

A position-time ($R-t$) plot of the position of the plume front was acquired using these images and is given in [Figure 12](#). The plume front is defined as the leading edge that exhibits 5% of the maximum emission intensity of the body of the plume. Uncertainty in the location from image to image is $\sim 10\%$. The plume front initially moves at $\sim 6 \times 10^6 \text{ cm/s}$. Consistent with our earlier observations [12], the initial 50 ns appears to exhibit no slowing of the plume front and the plume front position is linear in R . After this brief free expansion phase, the plume front in this pressure of He is expected to follow a shock wave expansion model with $R \sim t^{0.4}$. The solid line fits in [Figure 12](#) corresponds to the shock model.

We used imaging data for obtaining plume lengths at different laser intensity levels. These are very helpful for positioning the witness plate used for particle characterization as described in [Section IV.e](#).

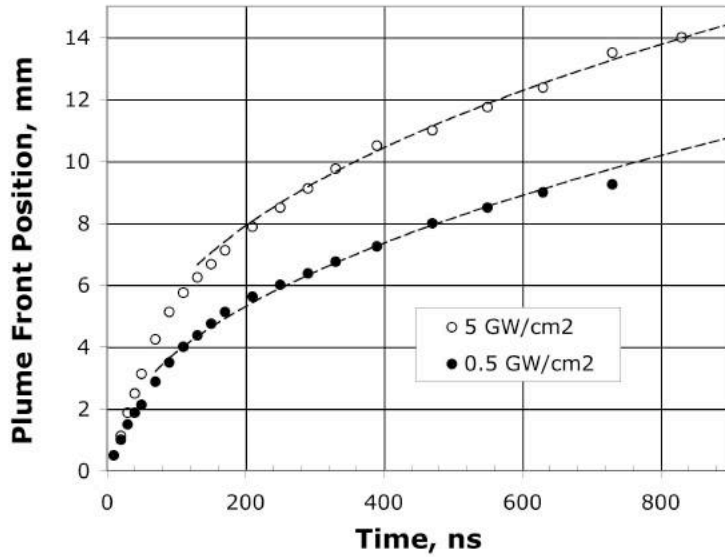


Figure 12. Position-time (R-t) plots of the luminous front of the Si ablation plume. The symbols in the figure represent experimental data points and the solid curves represent the shock wave model ($R \propto t^{0.4}$).

IV.b. Plasma temperature and density measurements

Due to theoretical uncertainties and strongly nonlinear physics, precise plume state variables (density, temperature, supersaturation and ionization fraction as a function of space and time) cannot be derived from theory in a reliable way; therefore, these parameters which are crucial for cluster formation and growth in laser plumes were measured experimentally and related to the final measured cluster size distribution.

For space and time resolved spectroscopy, an optical system was used to image the plasma plume onto the entrance slit of a spectrograph, so as to have one-to-one correspondence with the sampled area of the plume and the image. The optical system was translated to monitor different parts of the plume. Spatial resolution provided by our optical system was better than 0.5 mm. The exit port of the spectrograph was coupled to an ICCD camera that was operated with vertical binning to obtain spectral intensities versus wavelength. The spectrograph is equipped with 3 gratings (150 g/mm, 600 g/mm and 2400 g/mm).

The plasma temperature was measured using relative line intensities of silicon emission lines of the same ionization stage as described in ref. [32] from the hot plasma in the plume. For the temperature measurement we used the ratio of line intensities of singly charged silicon ions at 358.2 nm and 413.1 nm. For these measurements the gate of the intensifier was set at 5 ns. Figure 13 shows the plasma temperature decay as a function of time. An initial electron temperature of about 1 eV is observed with 5 GW/cm^2 and its value falls rapidly during the first 200 ns following termination of the laser pulse, dropping to a level of 0.3~0.4 eV. Initially the plasma expands isothermally within the duration of the laser pulse and adiabatically after the

termination of the pulse. During adiabatic expansion, the thermal energy is converted into kinetic energy and the plasma cools down very rapidly. Measurements at times less than about 40 ns are unavailable due to the large amount of continuum radiation present. Therefore, it is difficult for us to know with certainty the plasma temperature during and immediately following the laser pulse. This information would be useful for confirming the expansion dynamics, but is not needed to provide the information needed to describe the condensation physics, which begins *after* 50-100 ns (see below).

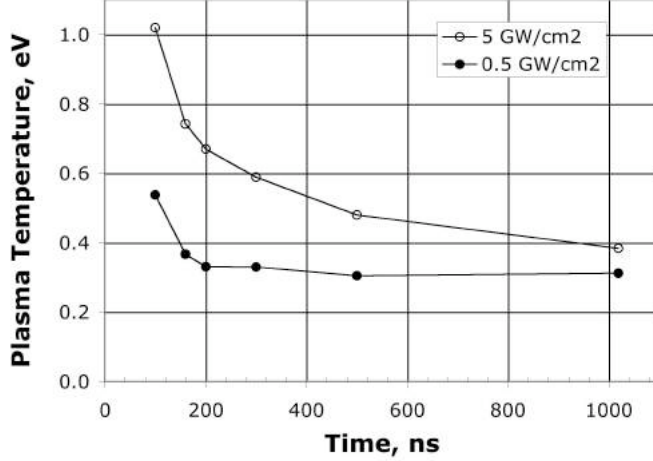


Figure 13. Time evolution of plasma temperature at 1 mm from the target.

For the estimation of electron density, the Stark broadened profile of the Si-I transition at 3905 Å was measured with the monochromator at its maximum resolution. The impact parameter of this line is obtained from ref. [33]. Besides Stark broadening, it is believed that only Doppler broadening contributes a significant amount to the total line width, which was found to be negligible in this experiment. Figure 14 shows the plasma density decay as a function of time. Similar to the temperature behavior, the plasma density decreases rapidly and reaches a plateau in the range of $5 \times 10^{16} \text{ cm}^{-3}$. As the plume density and temperature decrease, they reach values for which recombination is very slow and heat transfer is limited by conduction.

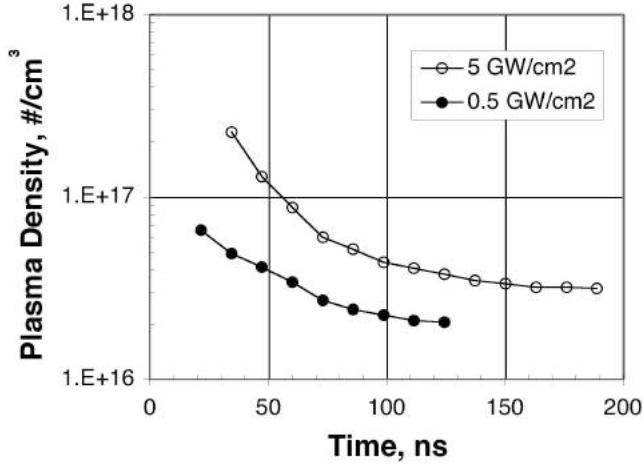


Figure 14. Time evolution of plasma density 1 mm from the target surface.

IV.c. Dimer spectroscopic results

A simple approximate measure of the onset of clustering in a plasma is the vibrational-electronic emission spectra from cluster species present in the plasma. These emissions result from the interaction of molecular vibrations with electronic transitions, which tend to give complex multi-line structures associated with a primary (0,0) transition usually associated with a neutral or unperturbed molecular state. These complex spectral emissions are explained in terms of the Frank-Condon principle, which states that an electronic transition takes place so rapidly that a vibrating molecule does not change inter-nuclear distance appreciably during any given transition. Hence, we observe many independent electronic emission lines associated with the many complex vibrational states of the molecular structure under study [34]. A typical emission spectrum of Si₂ observed during this experimentation can be seen in Figure 15.

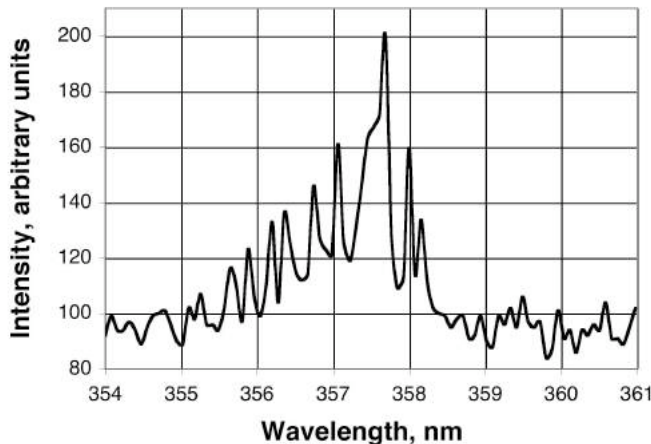


Figure 15 Typical molecular spectrum due to the presence of Si₂, taken at a distance of 10 mm from the target surface.

We measured the time resolved emission lines from different species in the laser plasma using a 5 nsec gated, intensified CCD. It showed that most of the line emission from the Si plume are due to Si⁺, Si⁺, Si and Si₂. The spectra indicate that a time delay exists for emission with respect to the incidence of the laser pulse. In addition, these measurements show that the emission lines from different emitting species are clearly related.

Figure 16 shows the emission intensity of Si⁺ and Si₂ for several laser intensities. In these data, it is apparent that a relationship exists between the ionic emission spectra in the plumes under study and the degree of vibrational emission observed in the same plasma [35]. For the runs at 5×10^7 W/cm², there is essentially no ionization signal, which remains constant barely above the thermal noise in the CCD. The runs at 5×10^8 W/cm² exhibit a significant signal from the Si⁺ line at $\lambda = 412.8$ nm which corresponds to the peak in Si₂ emissions observed at that intensity. The 5×10^9 W/cm² runs have approximately ten times that amount of emission for both Si₂ and Si⁺, and the same relationship is observed.

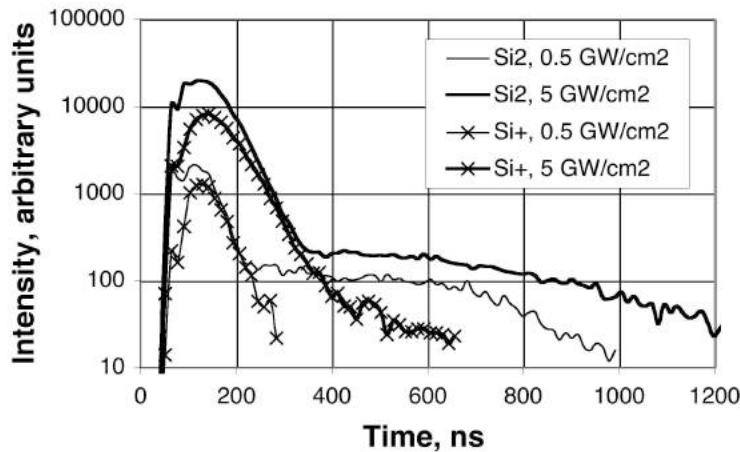


Figure 16. Si_2 vibrational emissions as a function of laser intensity and time in 500 mTorr He background collected at a distance of 10 mm from the target surface.

The formation of dimers can happen by one of two situations: either the dimers are formed in the presence of ions in densities proportional to the ion density, or a similar density of ions to dimers leaves the target surface initially [36]. It is unlikely that a significant number of dimers is emitted from the target surface because the bond energy of Si_2 is only about 1 eV [37], as compared with the first ionization energy of atomic silicon of 8.1 eV. Additionally, in the highly collisional early plasma immediately adjacent to the target surface, thermal equilibration happens extremely rapidly (on the order of a picosecond).

This point is also borne out when one examines the molecular, ionic and atomic spectra as a function of distance from the target at the higher laser intensities (5×10^8 – 5×10^9 W/cm²). We noticed at close distances most of the emission lines are due to ionic species. Any molecular emission from Si_2 species, if present, exists in such small amounts as to be indistinguishable from the continuum. At this point the emitting plasma is too hot to allow the formation of clusters. Further, if clusters were emitted directly from the surface at these intensities, one would observe molecular emission at this stage.

At greater distances Si_2 molecular emissions appear accompanied with Si^{++} , Si^+ and Si neutral atomic emissions. This makes sense when one considers the fact that the emitted plasma flows from the hot target into a cold background gas. In this case, one would expect to see a cooling at the leading edge of the plasma in contact with the background. This is caused by simple inter-diffusion with the cold background gas. Behind that leading edge, the plasma is cooled only through radiative emission and the work of expansion, therefore remains hotter and would be expected to contain species at a higher average temperature and ionization state.

Some interesting information regarding the onset and duration of nucleation also can be derived through these data when one remembers that the initial expansion velocity of the plasma plume at these laser intensities was on the order of 6×10^6 cm/s and there is no appreciable emission at the 2 mm location until about 50 ns and at that point in time, as previously described, there is no molecular emission noted. At the 6 mm location, which takes the plume about 100 ns to reach,

there are consistently distinct molecular emissions noted in the data. Overall, this means that the dimer emission probably begins in earnest sometime between approximately 50 and 100 ns.

Additionally, the duration of molecular emission provides some insight into the duration of cluster nucleation in the plasma. At 6 mm and 10 mm, the duration of molecular emission lasts about 400 and 800 ns respectively. That suggests the duration of the cluster birth phase in the plasma at these conditions is somewhere between 400 and 800 nsec. As previously mentioned, one would expect this birth phase to be followed by a phase which is dominated by heterogeneous cluster growth.

Overall, a number of conclusions can be drawn from these data. First, it is unlikely that dimers are emitted from the surface of the target, since molecular spectra are not observed near the target at any time. Second, ionic and molecular emission are seen to be coincident at distances farther from the surface of the target, which indicates that ions are present at the same time as clusters are initially formed. Finally, clustering in the plasma begins sometime between 40 and 100 ns and substantially decreases in about a microsecond, suggesting the bulk of cluster birth occurs relatively early in the expansion.

IV.d. Ionization and supersaturation

Spectroscopic measurements of plasma density and temperature allow us to approximate the saturation ratio and effective charge state. In order to proceed, we assume local thermodynamic equilibrium. Then, given an electron density and temperature, the neutral density is calculated using the Saha equation. The average charge state is given simply by n_e/n_o (*i.e.*, the maximum possible charge state for Si would be 14). In order to supplement our data at 0.5 and 5 GW/cm², we also derived and present the saturation ratio and ionization fraction at 50 GW/cm² using data from ref. [38]. That data was obtained using carbon expanding into He; however, the atomic number is sufficiently close that the trends appear to be consistent.

[Figure 17](#) shows the resulting saturation ratio at x=1 mm. Somewhat surprisingly, the saturation ratio *decreases* as the laser intensity *increases*. [Figure 18](#) shows the maximum charge state of the plasma as a function of laser intensity. The supersaturation data indicates an inverse relationship with increasing ionization fraction. Since supersaturation is the main variable upon which the condensation rate is dependent, that must be interpreted as a change in mechanism taking place with increasing ionization in the plasma; from homogeneous to heterogeneous condensation upon ions. Homogeneous condensation occurs at relatively large levels of supersaturation since, energetically speaking, it is a higher energy condensation pathway. Conversely, heterogeneous condensation is not associated with high levels of supersaturation as vapor atoms simply condense upon existing surfaces provided by the cluster-ion seedlings.

The results shown in [Figures 17 and 18](#) are consistent with our model predictions shown in [Figures 7 and 8](#). The saturation ratio in the plume is lower at higher laser intensities. In fact, at 50 GW/cm² the plume is sub-saturated at all times that we could measure (*i.e.*, the clusters should experience evaporation under these conditions). At reduced saturation ratio, one would expect the ion seed pathway to become more important; however, as the intensity continues to increase eventually condensation will stop due to high cluster temperature, heating by recombi-

nation, and the high expansion velocity which creates a very low vapor pressure in the plume. Modeling results predict an early spike in the saturation ratio even for this intensity, but our experimental data is limited to times greater than about 40 ns. It seems highly likely that condensation processes existed in the earliest stages of the plume expansion, since we measured a significant number of clusters on witness plates. These observations also agree with research results in the field of thin film deposition by PLD, where decreased condensate deposition is obtained using higher laser intensities [39].

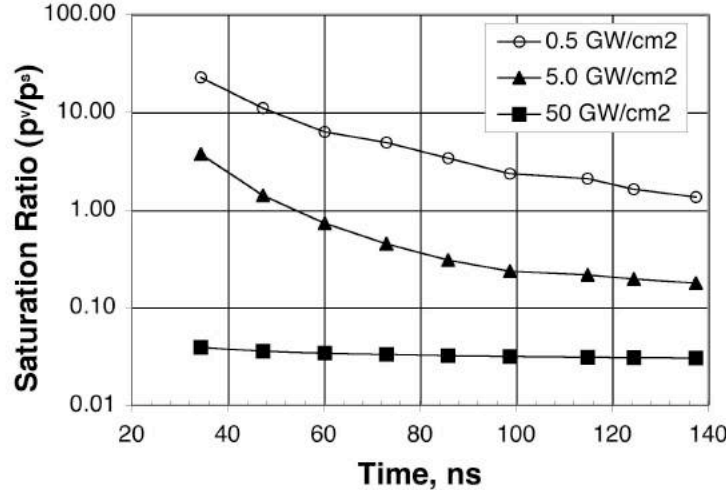


Figure 17. Saturation ratio at 1 mm, derived from spectroscopy and assuming LTE.

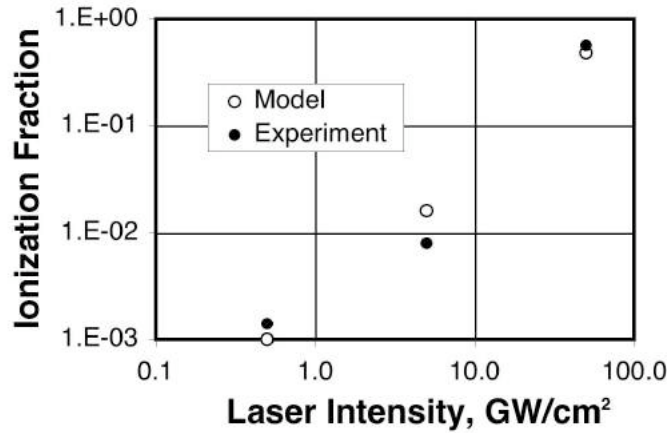


Figure 18. Maximum charge state at 50 ns, 1 mm from the target, as derived from spectroscopy and assuming LTE.

IV.e. Final Cluster size distribution

Nanoparticle diagnostics represent an active area of research and many methods have been used to attempt to measure the particulate size distribution of a sample of aerosol. These include use of a witness plate, differential mobility analyzer, laser induced incandescence, light scattering techniques *etc.* [21,40–43]. Witness plate methods coupled with atomic force microscopy offer

advantages over other methods in that they are relatively easily calibrated, offer reliable volume information and experimental simplicity enabling, in the present work, plasma state data to be easily taken simultaneously. Volume information is important because particulate morphology may not remain spherical, especially when clusters are collected in-situ at high velocity. In addition, when using witness plates one does not need to assume a predetermined size range for analysis as with other methods. The major downside associated with this approach is the need to fabricate atomic flatness witness plates in order to make reliable measurements. These plates must be carefully fabricated and handled to ensure their flatness and cleanliness.

Cluster size distributions were measured using atomic force microscopy on witness plates which were fabricated with near-atomic flatness. Witness plates were prepared starting with single crystal Si wafers. In order to achieve the flattest possible surface, the native oxide was stripped with HF and then, after cleaning, a controlled thermal oxide was grown at a temperature of 1350 K up to about 1 μm thickness. The resulting surface has a roughness of $\sim 4 \text{ \AA}$, which was verified using atomic force microscopy (AFM). The final step was to apply a metallic sputter coating of Au or Ta in order to allow us to perform SEM microscopy on the surface.

The witness plates were placed in the path of the expanding plumes at a distance close to the stagnation point predicted from our plume imaging results. This method, while far easier than in-situ diagnostics (based on light scattering for example), limits us to measuring only the final size distribution that reaches the plate. For all experiments, a control specimen was transported together with the test specimen throughout all stages of testing in order to verify the absence of contamination. Inside the test chamber the control specimen was masked to avoid coating with ablation products.

[Figures 19 and 20](#) show example results of AFM on specimens exposed to an average intensity of 5×10^8 and $5 \times 10^9 \text{ W/cm}^2$ respectively. All the experiments were performed at a helium pressure of 500 mTorr. Already from these nanographs, one can see clear evidence of the decrease in mean particle size with increasing laser intensity. [Figures 21-23](#) show histograms of the particle size distribution measured with AFM for three intensity levels, from 5×10^7 to $5 \times 10^9 \text{ W/cm}^2$. The histograms indicate that a relatively small decrease in mean particle size occurs in the lower intensity regime, but a fairly marked decrease occurs when the intensity increases from 5×10^8 to $5 \times 10^9 \text{ W/cm}^2$.

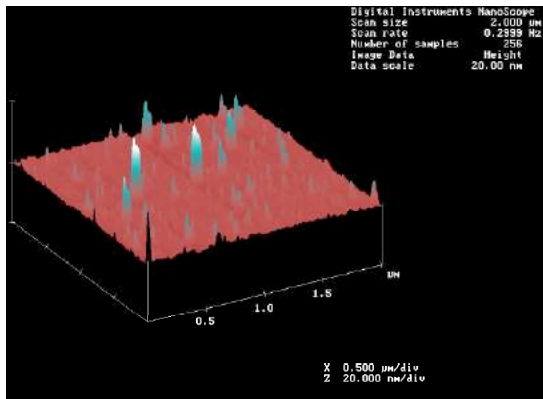


Figure 19. AFM result for $5 \times 10^8 \text{ W/cm}^2$.

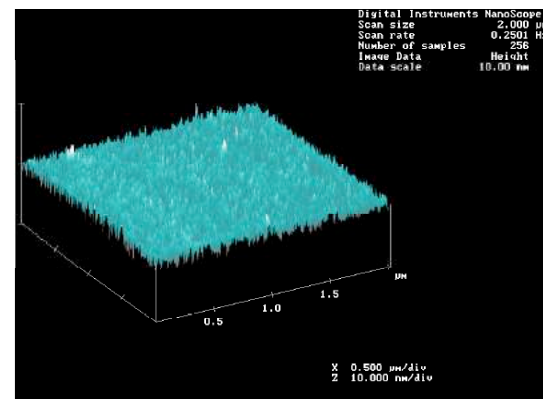


Figure 20. AFM result for $5 \times 10^9 \text{ W/cm}^2$.

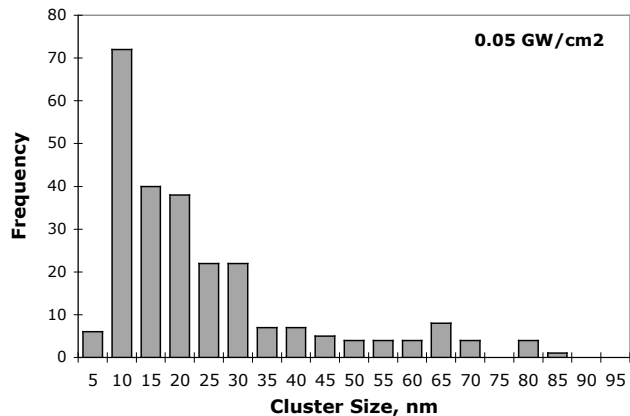


Figure 21. Cluster size histogram for 5×10^7 W/cm².

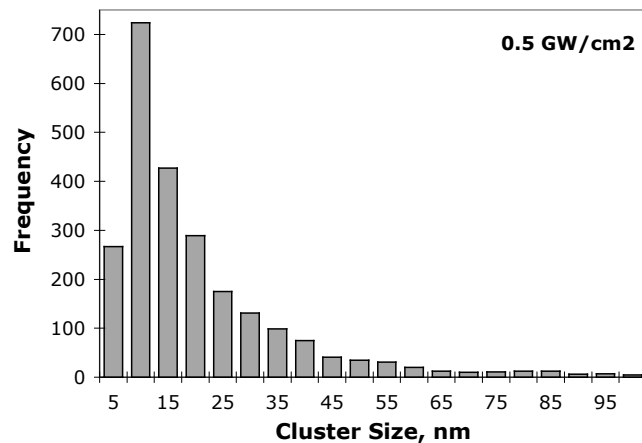


Figure 22. Cluster size histogram for 5×10^8 W/cm².

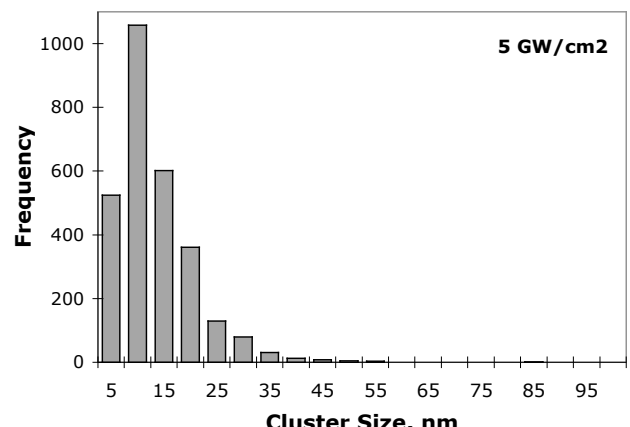


Figure 23. Cluster size histogram for 5×10^9 W/cm².

[Figure 24](#) summarizes the trend in average particle size with increasing laser intensity. In our work, the particle size distribution is found to decrease with increasing laser irradiance. Recently, Patrone *et. al* [44] observed mean cluster size is a growing function of laser fluence during ArF laser ablation of Si target at 4 Torr helium background pressure. They used the target itself as the witness plate and performed the experiments in small intensity range ($0.67\text{--}2.6 \times 10^8 \text{ W/cm}^2$) compared to present experiments. Moreover, the high background pressure used in their experiment support enhanced backflow of the species towards the target. In contrast, Seto *et. al* [45] observed the size of the nanoparticles generated by Si ablation using radiation from a frequency doubled Q-switched Nd:YAG laser decreases with increasing power density which is in agreement with the present experimental results. Their experimental conditions are similar to one used in the present studies, except the background pressure (5 Torr helium) and laser intensity range used ($2\text{--}8 \text{ GW/cm}^2$). This indicates that the size and spatial distribution of nanoclusters within the laser created plume are determined by the hydrodynamics of expansion and strongly depend upon the initial conditions, laser irradiance, and pressure of the background gas [46].

As can be seen in [Figure 24](#), the computational model diverges at the lower laser intensities. This may be due to the fact that in actuality there are a significant number of electrons present even at the lowest laser intensity level, which influence the nucleation processes in the plasma and decrease the average particle size. Since the model doesn't effectively represent these low levels of ionization, these electrons are not taken into account in the birth phase of the condensation process, hence the predicted particle size may be significantly inaccurate.

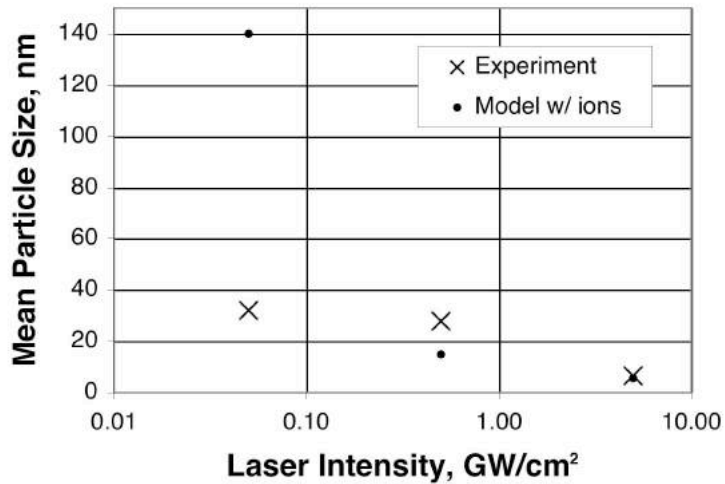


Figure 24. Comparison of experiments and modeling of mean cluster size vs. laser intensity

V. Summary and Conclusions

The influence of ionization on cluster formation in laser plasma was investigated experimentally and numerically. Ionization has been shown to be present in virtually all laser ablation plumes, even those only slightly above the ablation threshold. Due to the strong dependence, the condensation of virtually any practical laser plume takes place under the influence of ionization.

Although no single piece of data provides decisive proof, all evidence suggests that ionization plays a dominant role in the formation of clusters in laser ablation plumes. This evidence comes from fundamental theory, numerical modeling, and experimental measurements of the plume evolution and final condensate distribution.

Fundamental theory suggests that ions depress the formation energy of clusters due to dielectric attraction with surrounding vapor atoms, which increases the homogeneous nucleation rate by orders of magnitude. This leads to a larger number of seed sites during the cluster creation phase of the plume expansion and, consequently, smaller average cluster size after all of the vapor has condensed.

Numerical modeling of the temporal and spatial characteristics of the rapidly evolving ablation plume agrees with this first-principles prediction. Our modeling work had reasonable agreement in most cases with our experimental results. This agreement is facilitated by the fact that the target absorption depth and plasma recombination coefficient were derived *via* experiment. However, the nonlinearity of the physics associated with the formation of laser plasma and condensation makes this an extremely difficult and numerically unstable modeling task. Multiple levels of nonlinear interdependence exist in this problem; extreme care must be used to ensure numerical stability and a minimum of truncation error.

Due to our limited ability to model the complex nonlinear processes in a laser ablation plume, a comprehensive experimental approach was used to isolate and discern quantitative information on all variables related to cluster formation at one set of experimental conditions. In these experiments, laser intensity was employed as a means of varying the plasma ionization state. The data includes plume state variables, dimer and ion spectroscopy, and witness plate measurements of the final cluster size distribution.

Plasma spectroscopy was used to measure the plasma temperature and density, from which the degree of plume ionization and saturation ratio were derived. These measurements showed that the saturation ratio decreased with increasing laser intensity, whereas the charge state increased. At reduced saturation ratio, the ion seed pathway becomes more important, however eventually condensation will stop due to high cluster temperature, heating by recombination, and the high expansion velocity which creates a very low vapor pressure in the plume.

Spectroscopic investigation of the temporal and spatial variations of various species in the laser plasma suggest a correlation between the ionic, neutral and molecular spectral emissions emanating from the plasma. This understanding gives strong indication that the presence of ions is accompanied by nascent clusters in the form of Si₂, which strengthens the relationship between clusters and ions in both space and time. Questions still remain as to the exact nature of this coupling, which should be the subject of future investigations.

Silicon nanoclusters were captured on nanometer scale flat silicon witness plates by laser ablation of a (100) Si target. Witness plate substrates were read with an atomic force microscope to investigate final cluster distributions which were then correlated with plasma state parameters. The witness plate measurements clearly indicated an increase in the number density and decrease in average size of clusters formed as the laser intensity increased. This agrees with the

observation that ions increase the homogeneous nucleation rate, which leads to a larger number of smaller particles in the final condensate distribution.

Upon careful examination and integration of all the data collected throughout this work, a model describing cluster formation in which ions play an important role begins to emerge. First, the number of clusters formed is well correlated to the number of ions present in the system, which is precisely what one would expect if ions play a role in the condensation process. Second, the average cluster size decreases with increasing ionization fraction, which also makes sense if roughly the same amount of vapor is to be condensed onto a larger number of ion clusters. Third, the supersaturation data indicates an inverse relationship with increasing ionization fraction. Since supersaturation is the main variable upon which the condensation rate is dependent, that must be interpreted as a change in mechanism taking place with increasing ionization in the plasma; from homogeneous to heterogeneous condensation upon ions. Homogeneous condensation occurs at relatively large levels of supersaturation since, energetically speaking, it is a higher energy condensation pathway. Conversely, heterogeneous condensation is not associated with high levels of supersaturation because vapor atoms simply condense upon existing surface provided by the cluster-ion seedlings. Overall, a preponderance of the evidence suggests that the presence of ions is central to the formation of clusters in laser plasma.

References

1. D. B. Chrisey and G. K. Hubler, editors, *Pulsed Laser Deposition of Thin films*, John Wiley & Sons, Inc., New York, 1994.
2. D. B. Geohegan, A. A. Puretzky, G. Duscher, and S. J. Pennycook, "Time-Resolved Imaging of Gas Phase Nanoparticle Synthesis by Laser Ablation," *Appl. Phys. Lett.* **72**, 2987 (1998).
3. H. W. Kroto, J. R. Heath, S. C. O'Brien, R. F. Curl, and R. E. Smalley, "C60 Buckminsterfullerene," *Nature* **318**, 162-163 (1985).
4. M. Becker, J. Brock, H. Cai, D. Henneke, J. Keto, J. Lee, W. Nichols, and H. Glicksman, "Metal nanoparticles generated by laser ablation," *Nanostructured Materials*, **10** (5), 853-863 (1998).
5. M. Von Allmen, "Laser-Beam Interactions With Materials: Physical Principles and Applications," Springer, Berlin, 1987.
6. S. S. Harilal, C. V. Bindhu, V. P. N. Nampoori, and C. P. G. Vallabhan, "Influence of ambient gas on the temperature and density of laser produced carbon plasma," *Appl. Phys. Lett.* **72**, 167-169 (1998).
7. S. S. Harilal, "Expansion dynamics of laser ablated carbon plasma plume in helium ambient," *Applied Surface Science* **172**, 103-109 (2001).
8. D. B. Geohegan, in *Pulsed Laser Deposition of Thin Films*, edited by D. B. Chrisey and G. K. Hubler, John Wiley & Sons, Inc., New York, 115-165 (1994).
9. D. B. Geohegan and A. A. Puretzky, "Dynamics of laser ablation plume penetration through low pressure background gases" *Appl. Phys. Lett.* **67**, 197-199 (1995).
10. A. V. Bulgakov and N. M. Bulgakova, "Dynamics of laser-induced plume expansion into an ambient gas during film deposition," *J. Physics D* **28**, 1710-1718 (1995).
11. A. V. Bulgakov and N. M. Bulgakova, "Gas-dynamic effects of the interaction between a pulsed laser-ablation plume and the ambient gas: analogy with an underexpanded jet," *J. Physics D* **31**, 693-703 (1998).
12. S. S. Harilal, C. V. Bindhu, M. S. Tillack , F. Najmabadi and A. C. Gaeris, "Internal Structure and Expansion Dynamics of Laser Ablation Plumes into Ambient Gases," *J. Applied Physics* **93**(5), 2380-2388 (2003).
13. V. N. Rai, M. Shukla and H. C. Pant, "Effect of chamber pressure induced space charge potential on ion acceleration in laser produced plasma," *Laser and Particle Beams* **18** (2) 315-324 (2000).

14. K. R. Chen, J. N. Leboeuf, R. F. Wood, D. B. Geohegan, J. M. Donato, C. L. Liu, and A. A. Puretzky, "Accelerated Expansion of Laser-Ablated Materials near a Solid Surface," *Phys. Rev. Lett.* **75**(25), 4706-4709 (1995).
15. Y. Zeldovich and Y. Raizer. *Physics of Shock Waves and High-Temperature Hydrodynamic Phenomena*. Academic Press, 1967.
16. D. Kashchiev. *Nucleation: Basic Theory with Applications*. Butterworth Heinemann, Oxford, 2000.
17. A. C. Zettlemoyer (editor), *Nucleation*, Dekker, New York, 1969.
18. K. Russell, "Nucleation on gaseous ions," *J. Chemical Physics* **5**, 1809-1816 (1969).
19. B. Toftmann, J. Schou, T.N. Hansen, and J.G. Lunney, "Angular distribution of electron temperature and density in a laser-ablation plume," *Physical Review Letters* **84**(17), 3998-4001 (2000).
20. R.M. Mayo, J.W. Newman, A. Sharma, Y. Yamagata, and J. Narayan, "Electrostatic measurement of plasma plume characteristics in pulsed laser evaporated carbon," *Journal of Applied Physics* **86** (5), 2865-2871 (1999).
21. S. Tosto, "Modeling and computer simulation of pulsed-laser-induced ablation," *Applied Physics A: Materials Science & Processing* **68**(4), 439-446 (1999).
22. J.N. Leboeuf, K.R. Chen, J.M. Donato, D.B. Geohegan, C.L. Liu, A.A. Puretzky, and R.F. Wood, "Modeling of plume dynamics in laser ablation processes for thin film deposition of materials," *Physics of Plasmas* **3**(5), 2203-2209 (1996).
23. A. Gnedovets, A. Gusarov, and I. Smurov, "A model for nanoparticles synthesis by pulsed laser evaporation," *J. Phys. D: Appl. Phys.*, **32**, 2162-2168, 1999.
24. A. Gusarov, A. Gnedovets and I. Smurov, "Two-dimensional gas-dynamic model of laser ablation in an ambient gas," *Applied Surface Science* **154-155** (2000) 66–72.
25. H.C. Le, D.E. Zeitoun, J.D. Parisse, M. Sentis, and W. Marine, "Modeling of gas dynamics for a laser-generated plasma: Propagation into low-pressure gases," *Physical Review E* **62**(3), 4152-4161 (2000).
26. J. G. Collier, "*Convective Boiling and Condensation, 2nd Edition*," McGraw-Hill Book Company, New York, 1981.
27. C. J. Knight, "Theoretical Modeling of Rapid Surface Vaporization with Back Pressure," *AIAA Journal* **17**(5), 519-523 (1979).
28. I.C.E. Turcu, M.C. Gower, and P. Huntington, "Measurement of KrF Laser Breakdown Threshold in Gases," *Optics Communications* **134**(1-6), 66-68 (1997).

29. R. H. Griem, "High density corrections in plasma spectroscopy," *Phys. Rev.* **128** (1962) 997.
30. R. F. Wood , J. N. Leboeuf, D. B. Geohegan, A. A. Puretzky and K. R. Chen, "Dynamics of plume propagation and splitting during pulsed-laser ablation of Si in He and Ar," *Phys. Rev. B* **58** (3), 1533-1543 (1998).
31. J. Ferziger and M. Peric, "Computational Methods for Fluid Dynamics," Springer, Berlin, 1996.
32. H.R. Griem, *Principles of Plasma Spectroscopy*. 1997, New York: Cambridge.
33. H.R. Griem, *Plasma Spectroscopy*. 1964, New York: McGraw-Hill.
34. C. Banwell, *Fundamentals of Molecular Spectroscopy*. 1972, London: Mc-Graw Hill.
35. A. Douglas, "The Spectrum of Si₂ molecule," *Canadian Journal of Physics* **33** 801 (1955).
36. S.S. Harilal, R.C. Issac, C.V. Bindhu, V.P.N. Nampoori, and C.P.G. Vallabhan, "Temporal and spatial evolution of Ca in laser induced plasma from graphite target," *Journal of Applied Physics* **80**(6), 3561-3565 (1996).
37. A. Redondo, W.A. Goddard, and T.C. McGill, "Mott Insulator Model of the Si(111)-(2x1) Surface," *Journal of Vacuum Science & Technology* **21**(2), 649-654 (1982).
38. S.S. Harilal, C.V. Bindhu, R.C. Issac, V.P.N. Nampoori, and C.P.G. Vallabhan, "Electron density and temperature measurements in a laser produced carbon plasma," *Journal of Applied Physics* **82**(5), 2140-2146 (1997).
39. E. Riedo, F. Comin, J. Chevrier, F. Schmithusen, S. Decossas and M. Sancrotti, "Structural properties and surface morphology of laser-deposited amorphous carbon and carbon nitride films," *Surface and Coatings Technology* **125** (2000) 124–128.
40. S. Will, S. Schraml, K. Bader, and A. Leipertz, "Performance characteristics of soot primary particle size measurements by time-resolved laser-induced incandescence," *Applied Optics* **37** (24), 5647-5658 (1998).
41. D. B. Geohegan, A. A. Puretzky, G. Duscher, and S. J. Pennycook, "Photoluminescence from Gas-Suspended SiO_x Nanoparticles Synthesized by Laser Ablation," *Appl. Phys. Lett.* **73**, 438 (1998).
42. L. Landstrom, Z. Marton, N. Arnold, H. Hogberg, M. Boman, and P. Heszler, "In situ monitoring of size distributions and characterization of nanoparticles during W ablation in nitrogen atmosphere," *Journal of Applied Physics* **94**(3), 2011-2018 (2003).
43. A. R. Jones, "Light scattering for particle characterization," *Progress in Energy and Combustion Sciences* **25**, 1-53 (1999).
44. L. Patrone, D. Nelson, V. I. Safarov, M. Sentis, W. Marine, and S. Giorgio, "Photo-

- luminescence of silicon nanoclusters with reduced size dispersion produced by laser ablation," *J. Applied Physics* **87** (8), 3829-337 (2000).
45. T. Seto, Y. Kawakami, N. Suzuki, M. Hirasawa, S. Kano, N. Aya, S. Sasaki, and H. Shimura, "Evaluation of morphology and size distribution of silicon and titanium oxide nanoparticles generated by laser ablation," *Journal of Nanoparticle Research* **3**(2-3), 185-191 (2001).
46. B.S. Luk'yanchuk, W. Marine, and S.I. Anisimov, "Condensation of vapor and nanoclusters formation within the vapor plume, produced by ns-laser ablation of Si," *Laser Physics* **8**(1), 291-302 (1998).

List of Figures

1. Stages of laser ablation plume creation, expansion and condensation.
2. Free energy of cluster formation for Si at 2000 K and $n=10^{20}/\text{cm}^3$ compared with the same conditions with $Z_{\text{eff}}=0.01$.
3. Homogeneous nucleation rate both with and without ionization for the same parameters as [Figure 2](#).
4. Laser irradiance and surface temperature response.
5. Spatial distribution of vapor and background gas density at various times in the plume expansion.
6. Velocity profile at various times in the plume expansion.
7. Charge state evolution *vs.* time near the target surface.
8. Predicted evolution of the plume-averaged saturation ratio *vs.* time for several laser intensities.
9. Comparison of the predicted mean particle size after 500 ns both with and without ionization considered.
10. Chamber and diagnostic layout for ablation experiments (PTG, Programmable Timing Generator; WP, wave plate; R, reflector; BS, beam sampler; L, lens).
11. ICCD photographs of visible emission from laser-produced Si plasma at 5 GW/cm^2 average laser intensity and 500 mTorr He background gas. The timings in the images represent the time after the onset of plasma formation. All of the images are normalized to their maximum intensity. Plume behavior indicates free expansion.
12. Position-time (R-t) plots of the luminous front of the Si ablation plume. The symbols in the figure represent experimental data points and the solid curves represent the shock wave model ($R \propto t^{0.4}$).
13. Time evolution of plasma temperature at 1 mm from the target.
14. Time evolution of plasma density 1 mm from the target surface.
15. Typical molecular spectrum due to the presence of Si_2 , taken at a distance of 10 mm from the target surface.
16. Si_2 vibrational emissions as a function of laser intensity and time in 500 mTorr He background collected at a distance of 10 mm from the target surface.
17. Saturation ratio at 1 mm, derived from spectroscopy and assuming LTE.

18. Maximum charge state at 50 ns, 1 mm from the target, as derived from spectroscopy and assuming LTE.
19. AFM result for 5×10^8 W/cm².
20. AFM result for 5×10^9 W/cm².
21. Cluster size histogram for 5×10^7 W/cm².
22. Cluster size histogram for 5×10^8 W/cm².
23. Cluster size histogram for 5×10^9 W/cm².
24. Comparison of experiments and modeling of mean cluster size vs. laser intensity